



## ORIGINAL ARTICLE

# Effect of metal ions on structural, morphological and optical properties of nano-crystallite spinel cobalt-aluminate ( $\text{CoAl}_2\text{O}_4$ )



Monmon Podder<sup>a,b</sup>, Md. Farid Ahmed<sup>a,\*</sup>, Md. Rassel Moni<sup>b</sup>, Md. Lutfor Rahman<sup>a</sup>, Bristy Biswas<sup>a</sup>, Nahid Sharmin<sup>a</sup>

<sup>a</sup> Institute of Glass and Ceramic Research and Testing (IGCRT), Bangladesh Council of Scientific and Industrial Research (BCSIR), Dhaka 1205, Bangladesh

<sup>b</sup> Department of Chemistry, Comilla University, Cumilla 3506, Bangladesh

Received 14 November 2022; accepted 19 February 2023

Available online 23 February 2023

## KEYWORDS

$\text{CoAl}_2\text{O}_4$  nanoparticles;  
Sol-gel method;  
XRD;  
Color properties

**Abstract** The bright blue nano crystallite cobalt aluminate ( $\text{CoAl}_2\text{O}_4$ ) was synthesized by sol-gel method using a mixture of chelating agent of glycerol and citric acid. The effects of changing (0.05, 0.075, 0.10, 0.25, 0.50, and 0.75 mol/L) metal ion concentration on the structural, morphological and color properties of synthesized  $\text{CoAl}_2\text{O}_4$  were characterized by using X-ray diffraction (XRD), Scanning electron microscopy (SEM), Energy dispersive X-ray spectroscopy (EDX), Fourier transform infrared spectroscopy (FTIR), Nanoparticle size analyzer, Simultaneous Thermal Analyzer (STA), UV-vis absorption spectroscopy, and CIE-LAB colorimetric analysis. From the X-ray peak profile analysis, the crystallite size was measured by Debye-Scherrer (D-S) equation, and three different models presenting average crystallite sizes between 88.3 and 125.4 nm. The average lattice strain, dislocation density, lattice constant, cell volume, and zeta potential were between 0.00021 and 0.0058,  $(1.73 \text{ to } 12.8) \times 10^{14}$  (lines/m<sup>2</sup>), 8.10658 to 8.11181 Å, 533.60 to 533.81 Å<sup>3</sup>, -56.4 to -63.5 mV, respectively. Using UV-vis absorption spectroscopy, the band gap was calculated from Kubelka-Munk method, and the values of band gap increasing from 1.82 to 1.84 eV, respectively. The reflectance spectra and the CIE-L\*a\*b\* values of cobalt aluminate is also measured which confirmed the formation of blue nano crystallite cobalt aluminate.

© 2023 The Author(s). Published by Elsevier B.V. on behalf of King Saud University. This is an open access article under the CC BY license (<http://creativecommons.org/licenses/by/4.0/>).

\* Corresponding author.

E-mail address: [ahmedfarid@bcsir.gov.bd](mailto:ahmedfarid@bcsir.gov.bd) (M.F. Ahmed).

Peer review under responsibility of King Saud University.



Production and hosting by Elsevier

## 1. Introduction

Nano structured aluminates are a class of chemical compounds which have been the center of attraction for various applications due to their high thermal stability, chemical resistance, high quantum yield, low surface acidity, and large surface area (Sharma and Ghose, 2014; Ravikumar et al., 2015; Bayal and Jeevanandam, 2012). Spinel aluminates have a general formulae  $AB_2O_4$ , where A and B represent two different crystal sites of tetrahedral and octahedral structure, respectively, and the oxygen ions are arranged in a cubic closed structure (Gul et al., 2010; Tielens et al., 2006; Ballarini et al., 2009). The metal ion arrangements in spinels are the key factors contributing to its properties such as color, optical properties, catalytic activity, magnetic behavior, and diffusibility (Bersuker, 1996; Burns, 1993). Among these family of spinel aluminates, Cobalt aluminate ( $CoAl_2O_4$ ) has unique optical property, stable and resistant to light and weather. For these reasons, now a days researchers are trying to find out the best method of obtaining spinel structure which could be processed at an appropriate temperature by controlling homogeneity, purity, size and shape of the product, and thus be expected to control the color purity. This spinel Cobalt aluminate has found widespread use as a ceramic pigment (Burdett et al., 1982; Wang et al., 2006). The color of  $CoAl_2O_4$  is bright blue due to the electronic d-d transition of  $Co^{2+}$  in tetrahedral coordination and bright blue synthetic cobalt aluminate is called as Thernard's blue (Wang et al., 2016; Iakovleva, 2015; Zaharko, 2014; Xu 2015; Dumitru, 2017). Some author reported that calcination temperature is one of the factors that change the color properties of  $CoAl_2O_4$  (Taguchi, 2013). The synthesis method also influences the optical and catalytic properties and it has a significant effect on the crystallinity, purity, particle size, surface area and morphology of nano-crystalline  $CoAl_2O_4$  (Stringhini et al., 2014; Davar and Salavati-Niasari, 2011; Quirino et al., 2016). Due to the distribution of cations, spinels structure are classified into three types: normal, inverse and mixed spinels. Cobalt aluminate exhibits mostly as a normal spinel with  $Al^{3+}$  in octahedral sites and  $Co^{2+}$  in tetrahedral sites (Zayat and Levy, 2000). It has been extensively used in decoration, protective coatings, paint and coloration of ceramic particles (Zhang et al., 2017; Pan et al., 2015; Peymannia et al., 2014; Tong et al., 2016); fibres, glass, cement, rubber, glazes, paper, contrast enhancing luminescent pigment and ceramic bodies (Pan et al., 2015; Lewis, 1988; Alarcon et al. 1985; Jüstel et al., 1998). In addition,  $CoAl_2O_4$  is non-toxic inorganic nanoparticles and so it is an environmental friendly (Peymannia et al., 2014). The structural property of  $CoAl_2O_4$  makes it perfect for wide range of potential application in sensors, high density magnetic recording, magnetic fluids, microwave devices, absorbant materials and heterogeneous catalysis (Bid and Pradhan, 2003; Ayala and Marsh, 1991).

A variety of techniques have been applied for preparation of cobalt aluminate nanoparticles such as solid-state reaction (Srisawad et al., 2012), polymeric precursor method (Desouza, 2009), sol-gel method (Salavati-Niasari et al., 2009), co-precipitation method (Melo et al., 2003), hydrothermal method (Chen, 2004); dip coating (Grosso, 2011); etc. Methods have been reported to prepare  $CoAl_2O_4$  by reverse microemulsion using surfactant explaining as tedious process (Chandradass et al., 2010), by co-precipitation method preventing the aggregation to some extent which needs alkaline medium (Zhang et al., 2017), by sol-gel method mentioning that sol-gel method has better particle distribution and dispersity (Tang, 2017).

Sol-gel method is widely known as a simple, fast, high reproducible and low cost process for the production of pure nano structured cobalt aluminate powders (Salem et al., 2011; Salem et al., 2012; Salem, 2014) and the nano-particles formed with fast heating and compact reaction time (Ianoş et al., 2014; Ragupathi et al., 2014; Visinescu et al., 2011). Sol-gel method requires inorganic salt to prepare metal oxide sol by hydrolysis and poly-condensation reaction and the nano pigment cobalt aluminate powders were obtained after gelation and calcination process (Kurajica et al., 2012).

Cobalt aluminate nanoparticles were synthesized by a environment friendly method from tamarind fruit extract and developed a new and sustainable approach toward green chemistry (Mindru, 2019). Another synthesized method includes solution combustion by using Mentha piperita where aluminum nitrate and cobalt nitrate were used as reagent and Mentha piperita leaves extract as fuel and studied their photocatalytic activity on methylene blue (MB) under visible light irradiation (Gingas, 2021). Ioana Mindru et.al prepared the un-doped and  $Tb^{3+}$  doped calcium and strontium aluminates by using the tartarate multimetallic precursors and studied the effects of the preparation method on the structure, the morphology, the photoluminescence and thermoluminescence properties of  $CaAl_2O_4$ ,  $CaAl_2O_4:Tb^{3+}$ ,  $SrAl_2O_4$  and  $SrAl_2O_4:Tb^{3+}$  powders. (Mindru, 2017) (Fig. 1).

The key point of this study is to develop of  $CoAl_2O_4$  for using as blue pigment in ceramic ink and to know the effect of metal ion concentration on the structure, morphology, color properties and dispersion of  $CoAl_2O_4$ . In the current investigation,  $CoAl_2O_4$  nanoparticles have been synthesized through first and cheap Sol-Gel route where the  $Co^{2+}$  and  $Al^{3+}$  molar ratio was fixed at 1:2. The intermediate products were synthesized at six different concentrations of  $Co^{2+}$  and  $Al^{3+}$  ions and the consequences of thermal treatment have been explored by calcining the intermediate product at a fixed temperature.

## 2. Experimental

### 2.1. Chemicals and materials

Cobalt nitrate [ $Co(NO_3)_2 \cdot 6H_2O$ ], aluminum nitrate [ $Al(NO_3)_3 \cdot 9H_2O$ ], glycerol (GC,  $C_3H_8O_3$ ) and citric acid ( $C_6H_8O_7$ ) were purchased from Merck, Germany. Aqueous ammonia (25 wt %) was purchased from Merck, Mumbai. Deionized (DI) water was utilized in all experiments for making aqueous solution.

### 2.2. Sample preparation

Cobalt aluminate nano-crystallites were prepared by using different metal ion concentration denoted as S1 = 0.05, S2 = 0.075, S3 = 0.10, S4 = 0.25, S5 = 0.50, S6 = 0.75 m ol/L.

Aqueous solutions including highly pure salts of cobalt nitrate [ $Co(NO_3)_2 \cdot 6H_2O$ ] and aluminum nitrate [ $Al(NO_3)_3 \cdot 9H_2O$ ] with the molar ratio of 1:2 which were stirred for

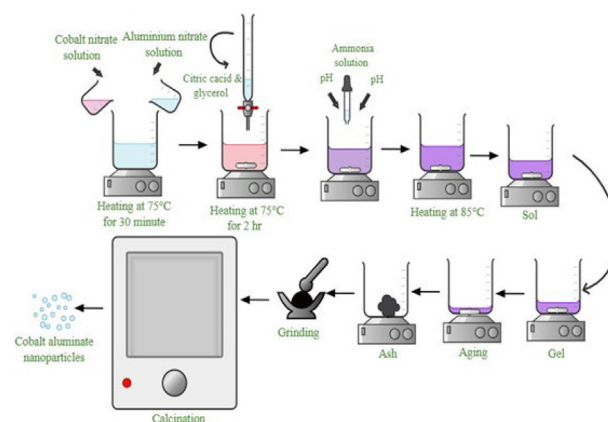


**Fig. 1** Schematic diagram for the preparation of cobalt aluminate nano-crystallites by sol-gel method.

30 min at 75 °C on the hotplate. A mixture of chelating agent, citric acid and glycerol with molar ratio of 1:1 was added into the mixed metal solution and the resultant solution was stirred for 2 hr with a magnetic stirrer. An ammonia solution was added dropwise to adjust the pH value to ~ 7.00 and the mixed solution was then allowed to evaporate at 85 °C on the hotplate with continuous stirring until a highly viscous gel was formed. Then the dry gel was placed in an oven at 110 °C for 5 h and black precursor was obtained. Finally, the resulting powder was calcined at desired temperature 1200 °C in a furnace for 4 h at the heating rate of 5 °C/ minute to obtain blue CoAl<sub>2</sub>O<sub>4</sub>.

### 3. Results and discussion

#### 3.1. X-ray diffraction (XRD) analysis

The phase composition of synthesized CoAl<sub>2</sub>O<sub>4</sub> was studied by X-ray Diffractometer (Smart Lab SE, Rigaku, Japan) by using Cu-K $\alpha$  radiation with scan speed 10°/ min in the range of 10° ≤ 2 $\theta$  ≤ 90°. In this analysis, the characteristic peaks of the samples were compared with the standard values (2 $\theta$ ) of cobalt aluminate. Different diffraction peaks were found in the pattern and the position of these peaks were very well matched that of the cubic CoAl<sub>2</sub>O<sub>4</sub> spinel according to JCPDS Card no.01-082-2242. Major peaks at (220), (311), (440), (511) and two weak peak at (400), (422) which confirm the presence of the single spinel phase. In this XRD analysis, no secondary phases were identified in any of the samples which indicates high purity and well crystallized of CoAl<sub>2</sub>O<sub>4</sub>. The XRD results showed similar pattern for all the samples which confirm that the change of metal ion concentration has no significant effect on the phase and stoichiometry of the prepared CoAl<sub>2</sub>O<sub>4</sub> nano-crystallites. Fig. 2. shows the XRD peaks of CoAl<sub>2</sub>O<sub>4</sub> spinel calcined at 1200 °C for 4 h.

The average crystallite size is determined by using the Debye-Scherrer and Wilson method, Williamson-Hall method, Halder-Wagner method and Size-Strain Plot method.

##### 3.1.1. Crystallite size and lattice strain determination

**3.1.1.1. The Debye-Scherrer and Wilson method.** The Debye Scherrer method, in X-ray diffraction and crystallography, is a technique to measure the crystallite size of the particles by peak broadening analysis (Sen et al., 2020). By this technique, the average crystallite size (D) is calculated from the full width at half maximum (FWHM) value of the highest peak by the Eq.(1).

$$D = \frac{k\lambda}{\beta_{D-S} \cos\theta} \quad (1)$$

Where, D<sub>D-S</sub> is the crystallite size (nm), k is the shape factor (k = 0.9),  $\lambda$  is the wavelength of Cu-K $\alpha$  radiation ( $\lambda = 0.154060$  nm),  $\beta_D$  is the internal breadth of the most intense peak FWHM (in radians) and  $\theta$  is the diffraction angle of Bragg.

The internal breadth can be calculated by rearranging the Eq. (1).

$$\beta_D = \frac{k\lambda}{D_{D-S} \cos\theta} \quad (2)$$

By Stokes and Wilson equation, the lattice strain of the sample can be expressed as (Stokes and Wilson, 1944)

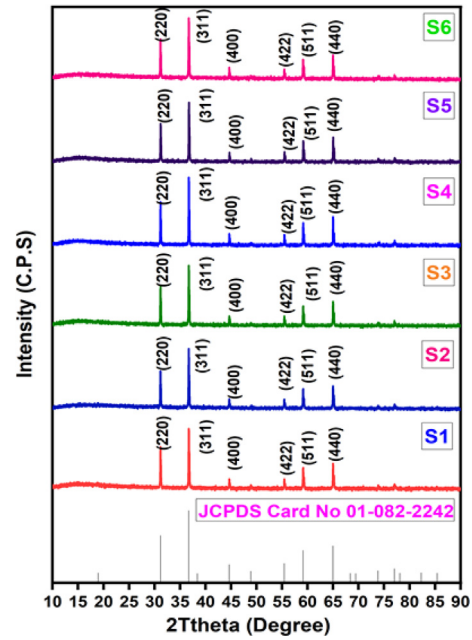


Fig. 2 XRD patterns of cobalt aluminate nano-crystallites calcinated at 1200 °C.

$$\epsilon = \frac{\beta_{strain}}{4 \tan\theta} \quad (3)$$

Where, lattice strain is denoted by  $\epsilon_{strain}$  and internal breadth for strain effect is denoted by  $\beta_{strain}$  (Sen, 2020). The values of average crystallite size (D<sub>D-S</sub>) and lattice strain ( $\epsilon$ ) are given in Table 1.

The crystallite size calculation using the Debye-Scherrer uses one single peak and then calculate the average crystallite size which presented the value from 96 to 153 nm. There might be some error to estimate the average crystallite size and similar types of errors are discussed in the literature (Hossain, 2022).

**3.1.1.2. Williamson-Hall method.** Williamson-Hall technique is an easiest integral breadth method where crystallite size and lattice strain dependent on the line broadening are differentiated by considering the peak breadth as a function of 2theta (Mote et al., 2012). The peak broadening observed from the lattice strain can be calculated with the help of Stokes-Wilson relation (Sen et al., 2020; Stokes and Wilson, 1944):

$$\beta_{strain} = 4\epsilon \tan\theta \quad (4)$$

The breadth of the observed peak is the addition of the of  $\beta_{strain}$  and  $\beta_D$

$$\beta_{hkl} = \beta_{strain} + \beta_D \quad (5)$$

Where,  $\beta_{hkl}$  is the full width at half maximum (FWHM) of a radiant peak,  $\beta_{strain}$  and  $\beta_D$  are the width due to size strain respectively. From the Eqs. (2) and (4) the value of  $\beta_D$  and  $\beta_{strain}$  putting in Eq. (5), we get,

$$\beta_{hkl} = 4\epsilon \tan\theta + k\lambda / D \cos\theta \quad (6)$$

Rearranging the Eq. (6),

$$\beta_{hkl} \cos\theta = 4\epsilon \sin\theta + k\lambda / D_{W-H} \quad (7)$$

**Table 1** The average crystalline size and lattice strain of the cobalt aluminate nano-crystallites by Debye-Scherrer and Wilson method, Williamson-Hall, Halder-Wagner and Size-strain plot.

Sample ID	D-S and Wilson method		W-H plot		H-W plot		SSP technique	
	$D_{D-S}(nm)$	Strain $\epsilon_W \times 10^{-3}$	$D_{W-H}(nm)$	$\epsilon_{W-H} \times 10^{-4}$	$D_{H-W}(nm)$	$\epsilon_{H-W} \times 10^{-4}$	$D_{SSP}(nm)$	$\epsilon_{SSP} \times 10^{-4}$
S1	101.41	0.58	240.63	0.81	197.00	0.70	197.00	0.70
S2	96.10	1.20	101.21	0.81	88.30	1.60	88.30	1.60
S3	97.89	1.09	96.29	0.23	95.60	1.50	95.60	1.50
S4	153.29	0.92	189.29	1.94	120.00	1.20	120.00	1.20
S5	110.11	1.07	103.47	2.21	101.00	1.40	101.21	1.40
S6	97.55	1.12	108.32	1.22	99.00	1.40	99.00	1.40

Eq. (6) follows the straight line equation,  $y = mx + c$ . By plotting the value of  $4\sin\theta$  along the x-axis and the value of  $\beta_{hkl}\cos\theta$  along the y axis (Yadav et al., 2016) in Fig. 3, the crystallite size and lattice strain of the synthesized six samples were estimated by the value of y-intercept and the slope of the straight line. The values of crystallite size ( $D_{W-H}$ ) and lattice strain ( $\epsilon_{W-H}$ ) using Williamson-Hall method are recorded in Table 1. The crystallite size calculated from this model were from 96 to 240 nm but too large crystallite size is not possible for the XRD technique using this instrument which made this

model invalid. And, similar types of large crystallite sizes are found in the literature which also explained as invalid model (Hossain et al., 2022). Using the W-H plot, the plotted straight lines are not well fit as the correlation co-efficient value of  $R^2$  is 0.00687, (-0.05015), (-0.11366), (-0.05252), (-0.14286), 0.00976 for sample S1, S2, S3, S4, S5, and S6, respectively.

3.1.1.3. Halder-Wagner method. By H-W analysis, the details about crystallite size ( $D_{H-W}$ ) and lattice strain ( $\epsilon_{H-W}$ ) of the nano-crystallites were measured from  $\beta_{hkl}$  and planar spacing

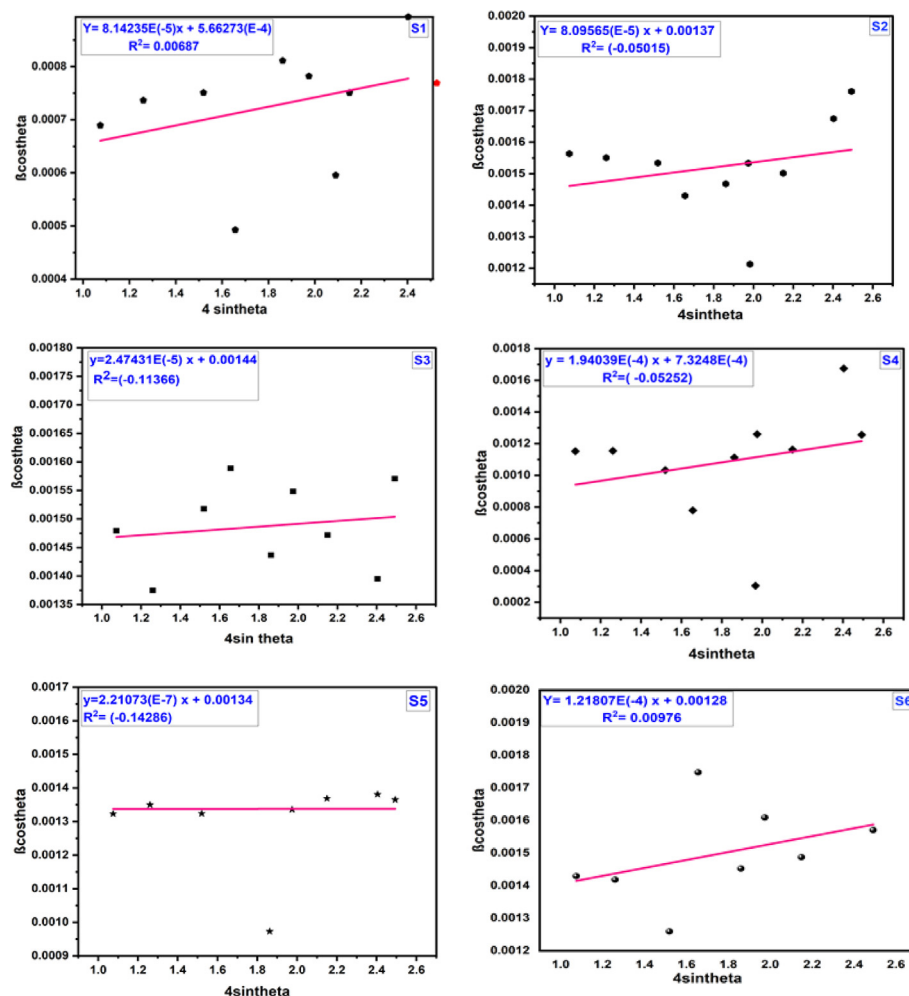


**Fig. 3** W-H plot of sample S1, S2, S3, S4, S5 and S6 Cobalt aluminate nano-crystallites.

$d_{hkl}$  (the length between near by planes in the set (h k l)) (Sen et al., 2020). Halder and Wagner given an alternative formula which contains  $\beta^*$  (integral width) of the reciprocal lattice point and  $d^*$ (interplanar spacing).

$$\left(\frac{\beta^*}{d^*}\right)^2 = \frac{k\beta^*}{D_{H-W}(d^*)^2} + (2\epsilon_{H-W})^2 \quad (8)$$

Where,

$$\beta^* = \frac{\beta \cos \theta}{\lambda} \quad (9)$$

$$d^* = \frac{2 \sin \theta}{\lambda} \quad (10)$$

By putting the value of  $\beta^*$  and  $d^*$  in Eq. (8) we get,

$$\left(\frac{\beta \cos \theta}{\sin \theta}\right)^2 = \frac{k\lambda}{D_{H-W}} \frac{\beta \cos \theta}{\sin^2 \theta} + 16\epsilon_{H-W}^2 \quad (11)$$

Rewriting the Eq. (11)

$$\left(\frac{\beta}{\tan \theta}\right)^2 = \frac{k\lambda}{D_{H-W}} \frac{\beta \cos \theta}{\sin^2 \theta} + 16\epsilon_{H-W}^2 \quad (12)$$

Eq. (11) resembles as  $y = mx + c$ , where slope =  $\frac{k\lambda}{D_{H-W}}$  and y intercept =  $16\epsilon_{H-W}^2$  (Sen, 2020). In H-W analysis, putting the value of  $\left(\frac{\beta}{\tan \theta}\right)^2$  along y axis and  $\frac{\beta \cos \theta}{\sin^2 \theta}$  along x axis which are shown in Fig. 4. The crystallite size and lattice strain observed from the slope and y intercept and listed in Table 1. Similar types of observation were found in the literatures (Leila et al., 2018). The straight lines plotted using H-W technique are good fit, as the correlation coefficient value of  $R^2$  is 0.96334, 0.99216, 0.99179, 0.94899, 0.97232, and 0.96274, respectively.

**3.1.1.4. Size-strain plot (SSP) method.** The SSP technique is used for isotropic crystal structure determination (Sen et al., 2020; Venkatalaxmi et al., 2004). The crystallite size described by a Lorentz function and the lattice strain explained by a Gaussian function (Kafashan, 2018; Ahemen et al., 2016) to check back W-H calculation. By this method, average particle size and strain of the nano crystallites can be estimated easily due to considering the SSP technique as isotropic. Eq. (13) can be used for determining the crystallite size and strain values of the nano crystallites with SSP method.

$$(d\beta \cos \theta)^2 = \frac{K}{D_{ssp}} (d^2 \beta \cos \theta) + \left(\frac{\epsilon_{ssp}}{2}\right)^2 \quad (13)$$

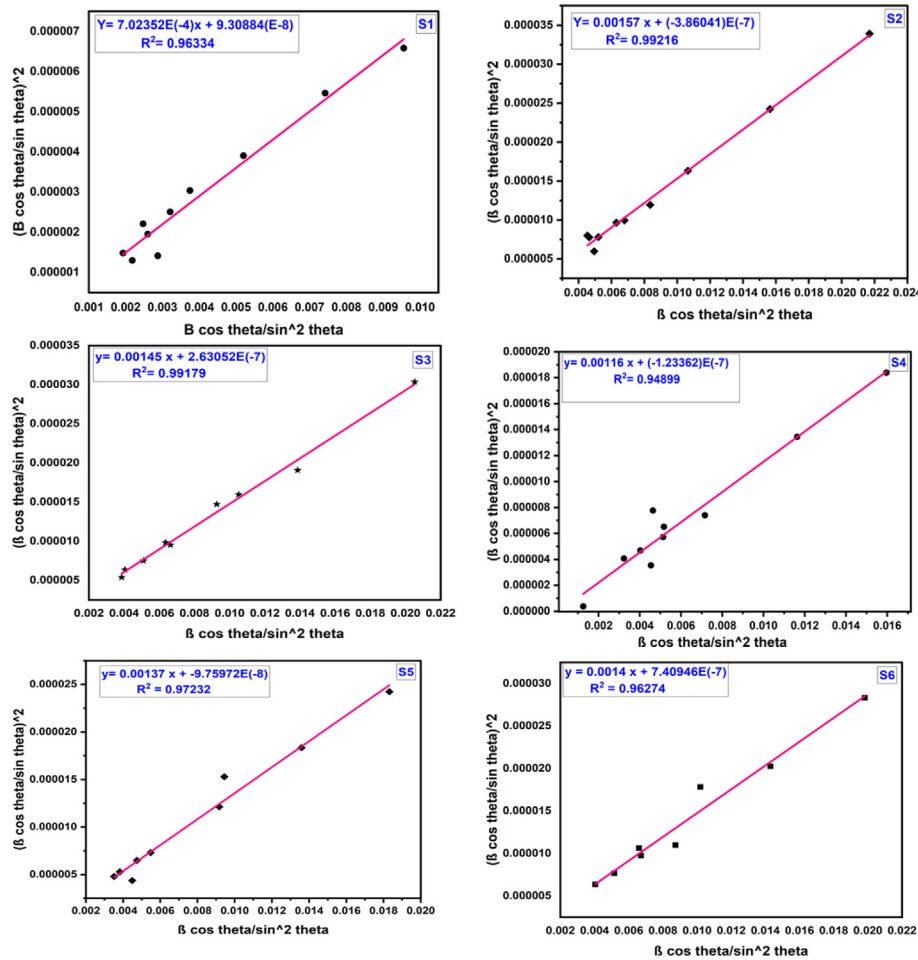


Fig. 4 H-W plot of Samples S1, S2, S3, S4, S5 and S6 cobalt aluminate nano-crystallites.

In Fig. 5, by plotting the values of  $(d^2\beta\cos\theta)$  along the x axis and  $(d\beta\cos\theta)^2$  along the y axis for all the samples, the crystallite size were estimated from the slope and lattice strain determined from the y-intercept of the linear extrapolated data (Mohammed et al., 2020) respectively and recorded in Table 1.

The straight lines plotted using SSP method are good fit, as the correlation coefficient value of  $R^2$  is 0.96317, 0.99216, 0.99179, 0.94899, 0.97232, 0.96275 respectively. The result which obtained from the SSP and H-W method is more correct than W-H method since the data more accurately fits in this method (Venkatalaxmi et al., 2004; Irfan et al., 2018). The results obtaining structural parameters are quite similar for SSP and H-W plot. So, it is clear that SSP and H-W method is the best method. The values of crystallite size and lattice strain for different metal ion concentration of  $\text{CoAl}_2\text{O}_4$  nano-crystallites from 4 different techniques are more or less similar. All the models used in the crystallite size calculation may not be applicable or fit for all the samples that is why different types of models are studied in this research work. The variation of the crystallite size are also reported in a number of literature (Hossain and Ahmed, 2022; Hossain et al. 2023; Hossain et al. 2022; Hossain et al. 2022; Tuntun et al., 2023). From the Table 1, it is observed that the sample S3 has the lowest crystallite size using all the methods.

### 3.1.2. Different microstructural parameters determination

The length of dislocation lines per unit volume of crystallite particle is called dislocation density ( $\delta$ ) that can be expressed as (Stokes and Wilson, 1944):

$$\delta = \frac{1}{D^2} \quad (14)$$

From the following Eqs. (15) and (16) the lattice constant of the nano crystallites has been estimated (Das, Jun. 2020). Here “d” is the interplanar spacing and n is the order of diffraction which is usually equal to 1 (Sen, 2020).

$$2d\sin\theta = n\lambda \quad (15)$$

$$a = d\sqrt{h^2 + k^2 + l^2} \quad (16)$$

Here, a is the lattice constant and the integers h, k and l are Miller indices of refractor planes (Boda, 2019; Durga Prasad and Hemalatha, 2019). The cube of the lattice constant “a” is expressed in Eq. (17) which is equal to the cell volume (Majid, 2020). Different microstructural parameters of 4 different method for different concentration of cobalt aluminate are recorded in Table 2.

$$V = a^3 \quad (17)$$

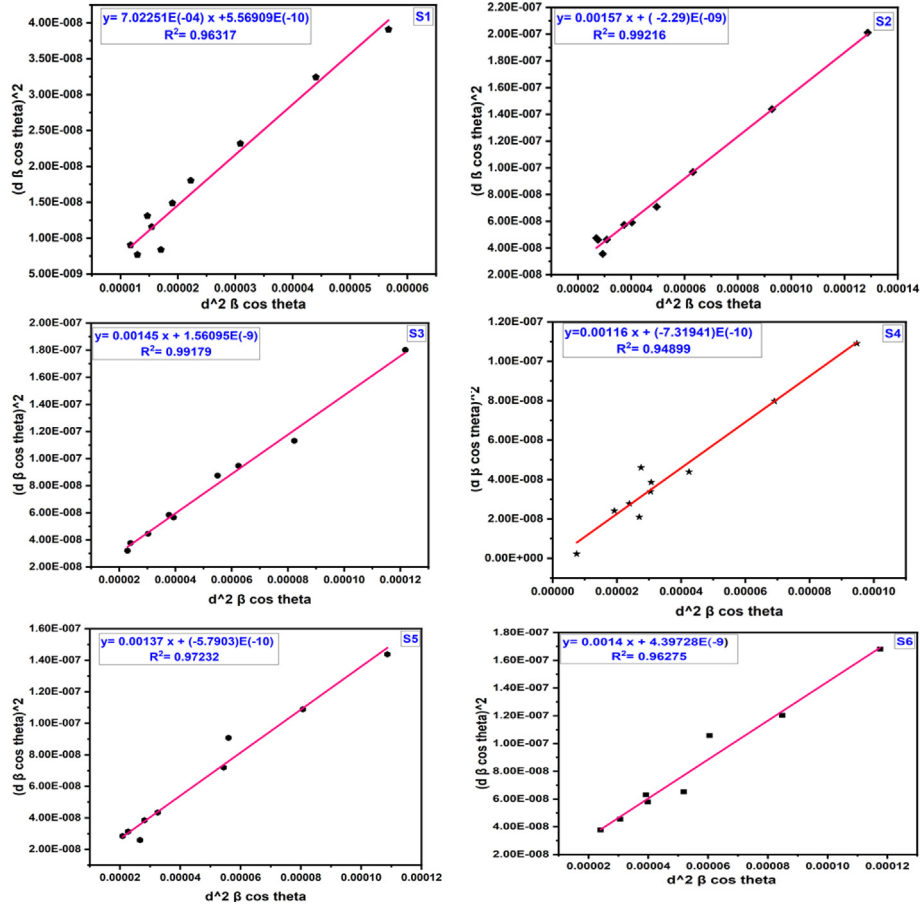


Fig. 5 SSP plot of S1, S2, S3, S4, S5, S6 cobalt aluminate nano-crystallites.

**Table 2** Effect of different method on various microstructural parameters.

Sample ID	Dislocation density, $\delta \times 10^{14}$ (lines/m <sup>2</sup> )				Lattice constant (Å)	Cell volume(Å <sup>3</sup> )
	D-S method	W-H plot	H-W plot	SSP method		
S1	10.30	1.73	2.58	2.58	8.11095	533.60
S2	11.50	9.76	12.80	12.80	8.11204	533.81
S3	9.02	10.80	10.90	10.90	8.11105	533.62
S4	6.34	2.79	6.94	6.94	8.10948	533.31
S5	8.70	9.34	9.80	9.80	8.10658	532.74
S6	9.59	8.52	10.20	10.20	8.11181	533.77

From the above Table 2, it is found that the value of dislocation density, lattice constant and cell volume calculated by all the four methods are very consistent with each other.

### 3.2. FTIR analysis

The FTIR analysis with different metal ion concentration of cobalt-aluminate was performed with a Fourier Transform Infrared Spectrometer (Model-IRAffinity-1S, MIRacle 10, Shimadzu, Japan). All the samples were showed almost the same FTIR absorption band shown in Fig. 6. Three frequency bands were detected at around 670, 560 and 460 cm<sup>-1</sup> respec-

tively which attributed the presence of CoAl<sub>2</sub>O<sub>4</sub> spinel (Duan et al., 2011).

The highest two bands observed at about 600 cm<sup>-1</sup> assigned to intrinsic stretching vibrations of M<sub>Tetrahedral</sub>-O bond at the tetrahedral site and the lowest band observed at about 400 cm<sup>-1</sup> is attributed to the octahedral M<sub>Octahedral</sub>-O bond stretching (Mazzoli and Favoni, 2012).

Similar results are also found in a study where the strong absorption bands at 667 cm<sup>-1</sup>; 475 cm<sup>-1</sup> and 418 cm<sup>-1</sup> show the formation metal oxide groups. In this, 667 cm<sup>-1</sup> of band appears indicates the formation of stretching vibrations of Co-O in the octahedral sites and 550 cm<sup>-1</sup> indicates the

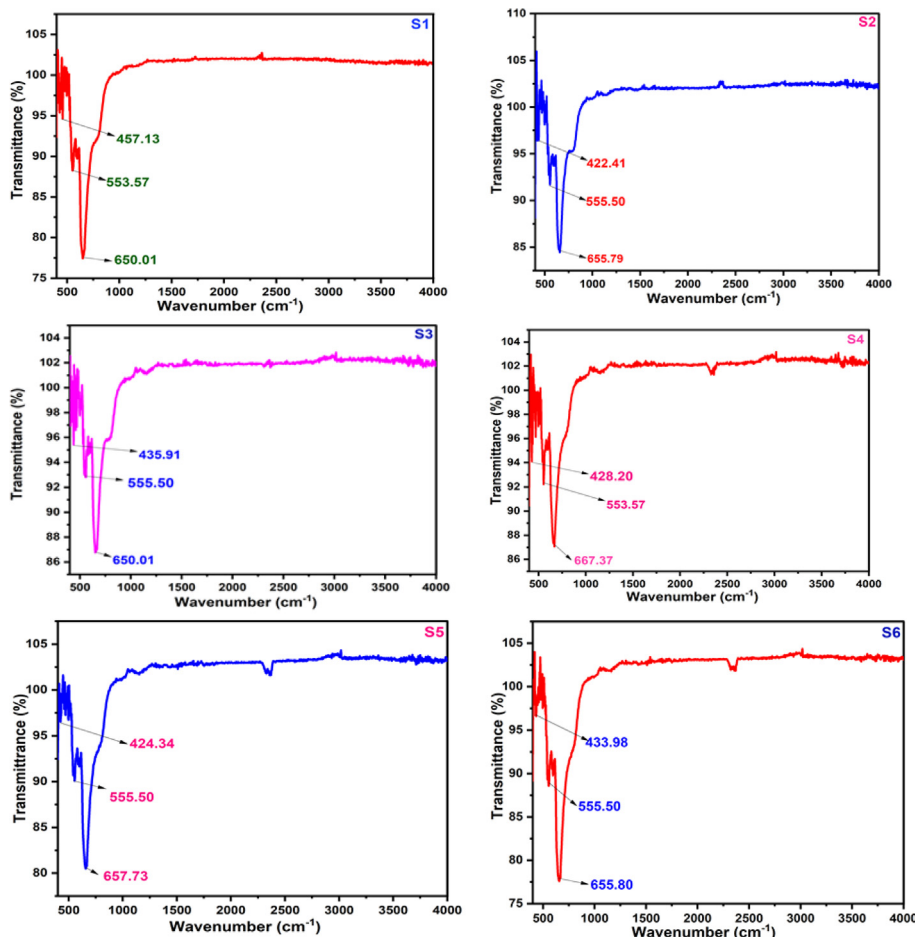


**Fig. 6** FTIR spectra of cobalt aluminate nano-crystallites.

stretching vibrations of Al-O in the tetrahedral sites (Venkatesan, 2022).

For all the samples, we get two strong bands around  $650\text{ cm}^{-1}$  and  $550\text{ cm}^{-1}$  which is responsible for intrinsic stretching vibrations of  $M_{\text{Tetrahedral}}\text{-O}$  bond at the tetrahedral site whereas the weak band at around  $420\text{ cm}^{-1}$  represents the octahedral  $M_{\text{Octahedral}}\text{-O}$  bond stretching.

### 3.3. Morphological analysis

The morphology of the synthesized  $\text{CoAl}_2\text{O}_4$  samples were analyzed with the help of Scanning Electron Microscopy (MA15 VP-SEM, Carl Zeiss Evo, UK). SEM images for all of the samples are shown in Fig. 7. SEM images reveal that the surface of the nano crystallites were huge agglomerated with different shape. The agglomerated property of  $\text{CoAl}_2\text{O}_4$  increased at higher temperature due to the increased surface energy and leading to large particle size. In the case of  $\text{CoAl}_2\text{O}_4$  powder, the low magnification FE-SEM image shows the presence of irregular aggregates (Mindru, 2019).

### 3.4. Compositional analysis:

The compositional analysis was obtained from EDX. The values of atomic weight percentage at 20 KeV for the  $\text{CoAl}_2\text{O}_4$

samples presented in Fig. 8 and Table 3. The atomic ratio of Co and Al for all the samples near the stoichiometric value of 0.5. The experimental ratio of Co:Al are close to 1:2. The EDX pattern of the  $\text{CoAl}_2\text{O}_4$  shows that the Co/Al ratio of S1,S2,S3,S4,S6 comparatively close to 0.5 except S5 sample. The major peaks of Co, Al and O exhibit the formation of  $\text{CoAl}_2\text{O}_4$  nano crystallites with no other impurities.

### 3.5. Zeta potential

Zeta( $\zeta$ ) potential of the cobalt-aluminate samples in liquid environment were estimated by Nanoparticle size Analyzer (nanoParticaSZ-100-S2, HORIBA scientific ltd, Japan) for measuring the dispersion stability. In this study, the samples were dispersed in 0.005 % de-ionized water solutions. To obtain the values of zeta potential, the samples were treated in neutral (pH  $\sim$  7) water suspension (Prabhakar and Samadder, 2018).

The results of zeta potential at different concentration are listed in Table 4 and are shown in Fig. 9. If the zeta potential value exists in the range (above + 30 mV and below -30 mV), the nano crystallite is said to be stable dispersion (Madhavi et al., 2013). In this analysis, all the samples were proved to be high dispersion stability in water. According to Ohshima's model, the zeta potential value is lower for large particles and higher for having smaller particle size. The reason is due

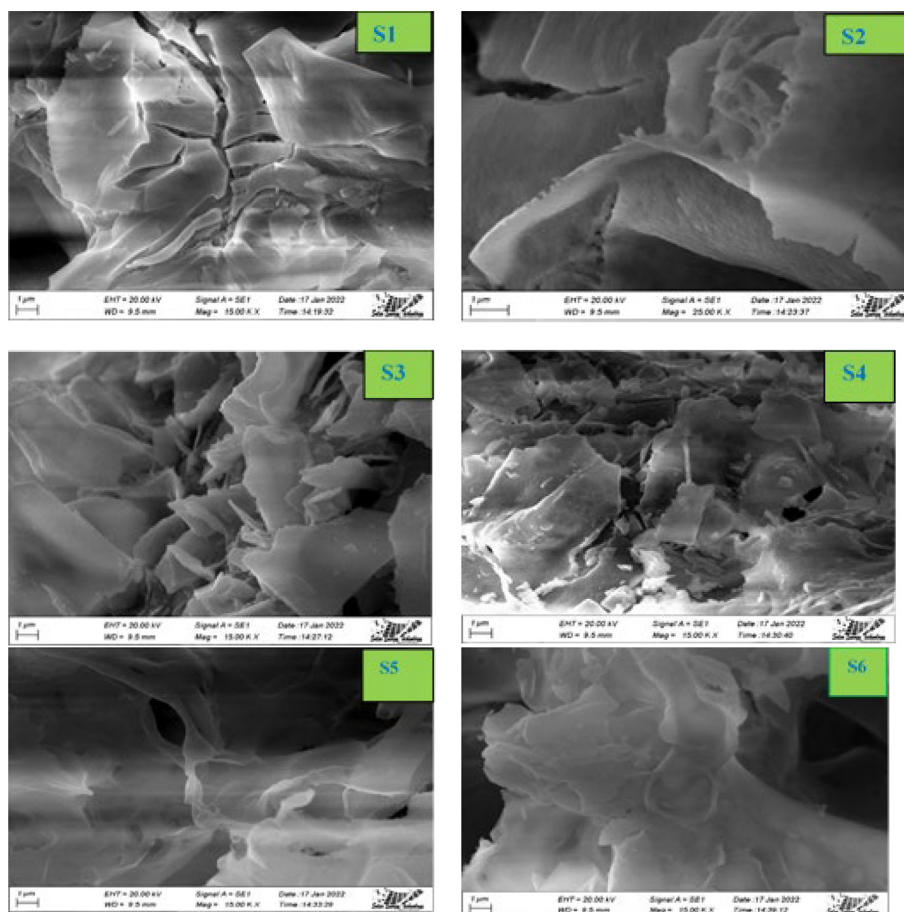


Fig. 7 SEM micrographs of  $\text{CoAl}_2\text{O}_4$  samples.

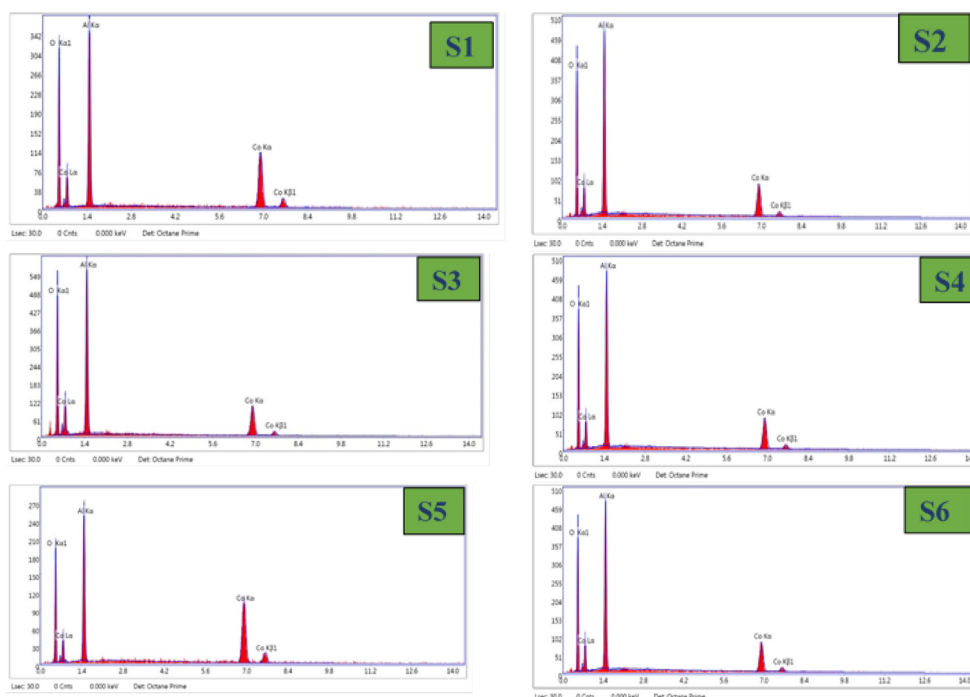


Fig. 8 EDS results of  $\text{CoAl}_2\text{O}_4$  nano-crystallites.

Sample ID	Atomic Weight (%)		Co/Al
	Co	Al	
S1	19.79	30.60	0.65
S2	12.14	29.78	0.41
S3	12.71	29.92	0.42
S4	13.31	30.29	0.44
S5	27.58	29.81	0.93
S6	13.34	30.47	0.44

Sample ID	Zeta potential (mV)
S1	-59.8
S2	-61.8
S3	-57.8
S4	-63.5
S5	-56.5
S6	-56.4

to the density of opposite charged ion for smaller particles is more intense than the particles having larger size (Holmberg et al., 2013). The highest zeta potential value (-63.5 mV) is obtained for the sample S4. It may be possible due to the particle size of these sample may be smaller than the other synthesized samples.

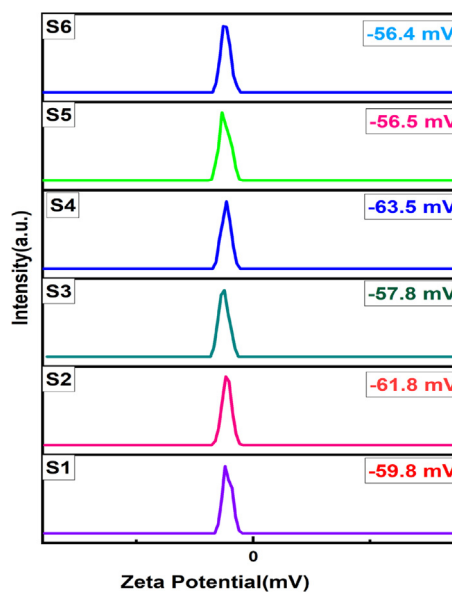


Fig. 9 Zeta potentials results of S1, S2, S3, S4, S5 and S6 samples.

### 3.6. Particle size analysis

The size distribution of the synthesized cobalt-aluminate particles in the solution form were analyzed at 22.5 °C using a Nanoparticle Size Analyzer (nanoParticaSZ-100-S2, HORIBA scientific ltd, Japan). Particle size were measured using dynamic light scattering method. The resultant particle size distribution of cobalt-aluminate nano crystallites are presented in Table 5. The synthesized products were dispersed in 0.005 % water solution and nano-particles analyzer gives hydrody-

**Table 5** Particle size distribution results of cobalt aluminate particles.

Sample ID	Average Particle Size (nm)
S1	3602.4
S2	2901.3
S3	3450.7
S4	2887.5
S5	3390
S6	3243

dynamic diameter which is always higher than the other dehydrated diameter (de la Calle et al., 2019; Bootz et al., 2004). The average particle size decreases from (3602–2887 nm) with the increasing of metal ion concentration. The particles remained in the cluster form which increased the size of hydrodynamic volume and the aggregated particles were also visualized in the SEM image.

### 3.7. Thermal analysis

The thermogravimetric analysis (TGA) and Differential scanning calorimetry (DSC) have been carried out by using a NETZSCH STA 449 F5 simultaneous thermal analyzer (STA) under nitrogen atmosphere with heating rate of 10 K/min. Fig. 10. exhibits the thermogravimetric character of the samples before calcination from room temperature to 1200 °C.

The investigation confirms the  $\text{CoAl}_2\text{O}_4$  formation as decomposition product with total 50 % weight loss. The first weight loss of about 4.15 % occurred in the range of 30–205 °C due to the loss of interstitial water. The second weight loss of about 3.93 % attributed in the range of 205–380 °C due to the loss of co-ordinated water. The significant weight loss of about 13.14 % occurs in the range of 380–580 °C may be due to the decomposition of citrate and nitrate ions. The temperature higher than 580 °C, the weight loss corresponds to the reduction of  $\text{Co}^{3+}$  to  $\text{Co}^{2+}$  in the presence of residual carbon and spinel  $\text{CoAl}_2\text{O}_4$  was formed (Dumitru, 2017). From DSC data curve an exothermic peak is found at 723 °C which is occurred during the formation of cobalt aluminate.

### 3.8. Optical property of $\text{CoAl}_2\text{O}_4$

#### 3.8.1. Color and reflectance spectra of $\text{CoAl}_2\text{O}_4$

UV-visible Spectrophotometer (Perkin Elmer Lambda 1050<sup>+</sup>) was used to determine the color factors  $L^*$ ,  $a^*$  and  $b^*$ . The col-

**Table 6** CIE- $L^*a^*b^*$  values of cobalt aluminate nano crystallites with different metal ion concentration.

Sample ID	$L^*$	$a^*$	$b^*$	Chroma
S1	61.72	1.59	-19.55	30.07
S2	59.60	-0.01	-13.72	29.92
S3	59.20	1.50	-19.18	29.67
S4	58.49	-0.15	-17.63	26.48
S5	60.49	-0.19	-16.48	26.48
S6	61.18	0.23	-15.96	29.45

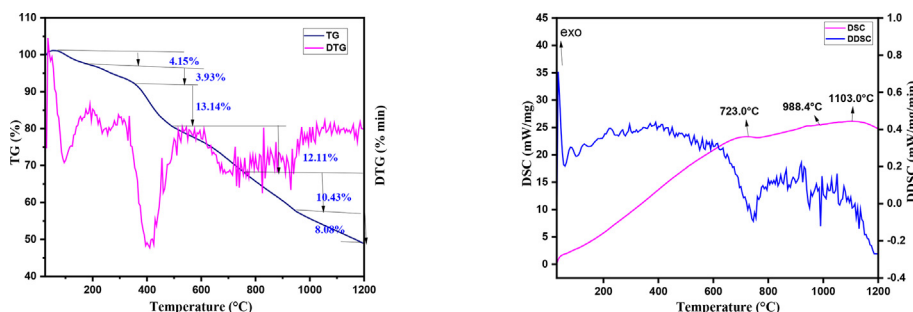
orimetric data of CIE- $L^*a^*b^*$  values in Table 6 summarized the color performance of the particles. The blue color was mainly denoted by the parameter  $b^*$  value and the more the magnitude of the negative value the more bluer the sample. It can be seen that with the increasing of metal ion concentration, the  $b^*$  value gradually decreased from (-19.55 to -15.96) and its chroma also decreased from 30.07 to 29.45. This means that the metal ion concentration had a significant effect on color properties of the resulting nano crystallites and it was found that S1 sample at 0.05 mol/L corresponded more to blue color ( $b^* = -19.55$ ) and its saturation is 30.07 indicating that the samples S1 represents high color purity and brightness. The changes in a certain amount of the Co concentration, the crystal lattice structure of  $\text{CoAl}_2\text{O}_4$  will exhibit distortion, including Co with coordination tetrahedral as the center. The density of electron cloud in the 3d orbital of Co has also great influence, which changes the level of energy splitting and the pigment color. The reflectivity of the cobalt aluminate nano crystallites was observed in the visible wavelength range and shown in Fig. 11. The intensity of the reflection peak of cobalt aluminate at 400–492 nm (blue) was decreased significantly with the increasing of metal ion concentration which is congruous with the colorimetric data (Song et al., 2017).

#### 3.8.2. Band gap energy

The band gap of all the synthesized samples were carried out in solid powder form by using UV-visible Spectrophotometer (Perkin Elmer Lambda 1050<sup>+</sup>).

The optical band gap energy ( $E_{\text{gap}}$ ) of synthesized cobalt aluminate was determined by Kubelka-Munk (K-M) function as follows:

$$F(R) = \frac{(1 - R)^2}{2R} \quad (18)$$

**Fig. 10** Thermal behaviour of the S6 sample before calcination (A) TGA, and (B) DSC.

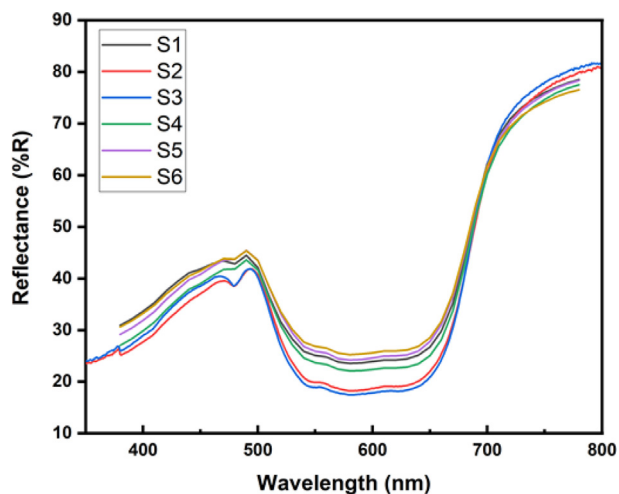


Fig. 11 Reflection spectra of  $\text{CoAl}_2\text{O}_4$  nano crystallites in the visible wavelength range.

Where,  $F(R)$  stands for Kubelka-Munk function and  $R$  is related to the percentage reflectance. The Kubelka-Munk function is related to the absorption co-efficient of the material.

$$F(R) \propto \alpha = \frac{(h\nu - E_{\text{gap}})^n}{h\nu} \quad (19)$$

Where,  $E_{\text{gap}}$  is the band gap energy,  $h\nu$  is the incident photon energy,  $n$  is the optical transition process. For the direct allowed transition, the value of  $n$  is considered as  $1/2$ . The energy band gap calculated by plotting  $(\alpha h\nu)^2$  against  $h\nu$  is shown in Fig. 12. (Debnath and Das, 2020). In semiconductors, the energy band gap plays a important role, from which we can find out the application in the optoelectronic devices. The direct band gap value of the undoped  $\text{CoAl}_2\text{O}_4$  was observed to be 1.82–1.84 eV which is lesser than the reported value of pure cobalt aluminate i.e., 2.57 eV (Dash et al., 2021). There is no significant changes are found in the calculation of band gap energy. Though there is a small variation in the band gap energy, this may be due to the manual calculation from the plot.

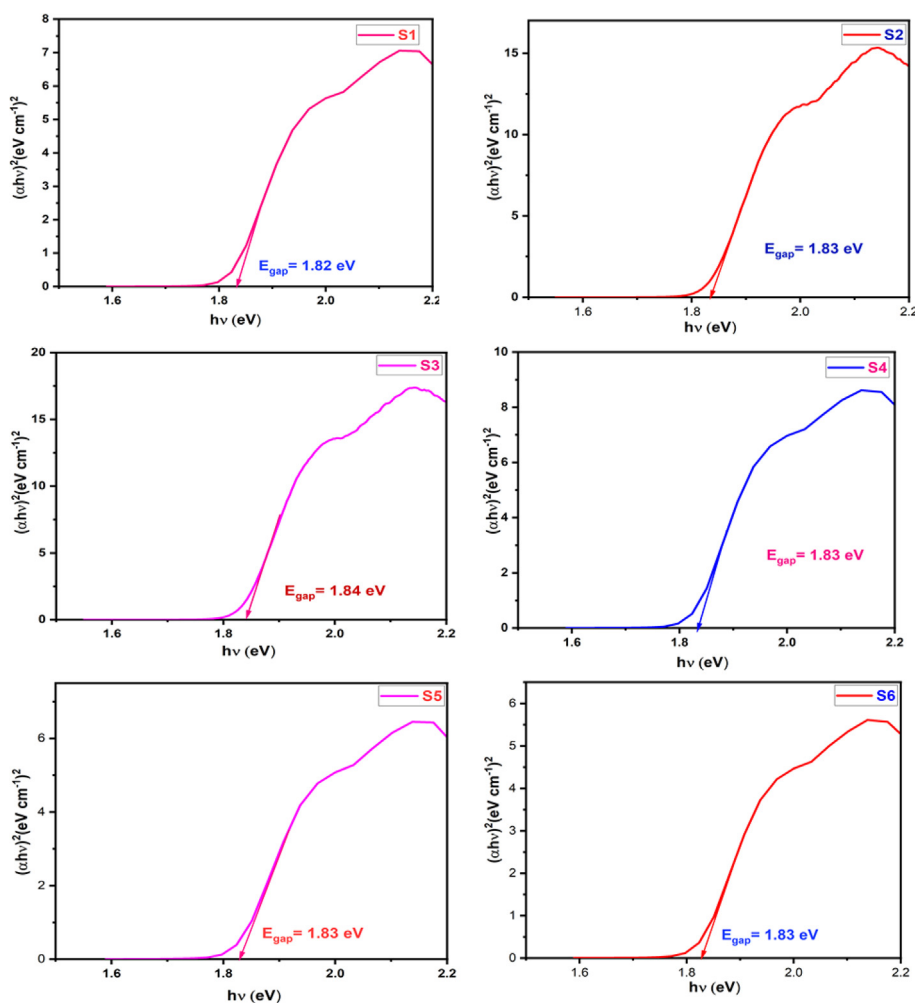


Fig. 12 Optical band gap energy calculated from Kubelka-Munk method for cobalt aluminate.

#### 4. Conclusion

Nano crystalline cobalt aluminate ( $\text{CoAl}_2\text{O}_4$ ) was prepared successfully with varying metal ion concentration by sol-gel method with a calcination temperature of  $1200^\circ\text{C}$  for 4 hr which was confirmed by XRD, FTIR, SEM, EDX, UV-vis, etc. The lowest crystalline size (95–97 nm) obtained for the sample, where metal ion concentration was 0.10 mol/L, using four different models. The zeta potential results of the S4 (0.25 mol/L) sample in aqueous solution was obtained as  $-63.5$  mv, indicating that the sample has better dispersion stability than other synthesized samples, which will be demanding in the application sector of ceramic ink. The parameter  $b^*$  value gradually decreased with the increasing of metal ion concentration, and the colorimetric data presented that the  $b^*$  value of the S1 sample could be reached as high as  $(-19.55)$  at  $1200^\circ\text{C}$ . The saturation (30.07) revealed that the sample S1 (0.05 mol/L) represented high color purity as well as brightness. The band gap values (1.82–1.84 eV) indicated a small changes when metal ion concentrations were varied.

#### CRediT authorship contribution statement

**Monmon Podder:** Investigation, Formal analysis, Software, Data curation, Writing – review & editing, Writing – original draft. **Farid Ahmed:** Conceptualization, Methodology, Resources, Supervision, Project administration, Visualization, Writing – review & editing. **Rassel Moni:** Validation, Resources, Writing – review & editing. **Lutfor Rahman:** Validation, Resources, Writing – review & editing. **Bristy Biswas:** Validation, Resources, Writing – review & editing. **Nahid Sharmin:** Project administration, Supervision, Writing – review & editing, Funding acquisition.

#### Declaration of Competing Interest

The authors declare that they have no known competing financial interests or personal relationships that could have appeared to influence the work reported in this paper.

#### Acknowledgements

This work was supported by the Ceramic Raw Materials & Ceramic Materials Testing Division, Institute of Glass and Ceramic Research & Testing (IGCRT), Strengthening of Institute of Glass and Ceramic Research & Testing (SIGCRT) project, Glass Research Division, IGCRT and Institute of Fuel Research & Development (IFRD), Bangladesh Council of Scientific and Industrial Research (BCSIR), Dhaka, Bangladesh.

#### References

- Ahemen, I., De, D.K., Dejene, F.B., Viana, B., 2016. White light tunable emissions from ZnS: Eu<sup>3+</sup> nanophosphors over 330–465 nm excitation range for white LED applications. *Mater. Res. Express* 3, (4). <https://doi.org/10.1088/2053-1591/3/4/045016>
- Alarcon, J., Escribano, P., Marin, R.M., 1985. Co (II) based ceramic pigments. *Br. Ceram. Trans. J.* 84 (5), 170–172.
- Ayala, R.E., Marsh, D.W., 1991. Characterization and long-range reactivity of zinc ferrite in high-temperature desulfurization processes. *Ind. Eng. Chem. Res.* 30 (1), 55–60. <https://doi.org/10.1021/ie00049a009>.
- Ballarini, N., Cavani, F., Passeri, S., Pesaresi, L., Lee, A.F., Wilson, K., 2009. Phenol methylation over nanoparticulate  $\text{CoFe}_2\text{O}_4$  inverse spinel catalysts: the effect of morphology on catalytic performance. *Appl. Catal. A: General* 366 (1), 184–192. <https://doi.org/10.1016/j.apcata.2009.07.003>.
- Bayal, N., Jeevanandam, P., 2012. Synthesis of metal aluminate nanoparticles by sol-gel method and studies on their reactivity. *J. Alloy. Compd.* 516, 27–32. <https://doi.org/10.1016/j.jallcom.2011.11.080>.
- Bersuker, I.B., 1996. *Electronic structure and properties of transition metal compounds: introduction to the theory*. Wiley, New York.
- Bid, S., Pradhan, S.K., 2003. Preparation of zinc ferrite by high-energy ball-milling and microstructure characterization by Rietveld's analysis. *Mater. Chem. Phys.* 82 (1), 27–37. [https://doi.org/10.1016/S0254-0584\(03\)00169-X](https://doi.org/10.1016/S0254-0584(03)00169-X).
- Boda, N. et al, Mar. 2019. Effect of rare earth elements on low temperature magnetic properties of Ni and Co-ferrite nanoparticles. *J. Magn. Magn. Mater.* 473, 228–235. <https://doi.org/10.1016/j.jmmm.2018.10.023>.
- Bootz, A., Vogel, V., Schubert, D., Kreuter, J., 2004. Comparison of scanning electron microscopy, dynamic light scattering and analytical ultracentrifugation for the sizing of poly(butyl cyanoacrylate) nanoparticles. *Eur. J. Pharm. Biopharm.* 57 (2), 369–375. [https://doi.org/10.1016/S0939-6411\(03\)00193-0](https://doi.org/10.1016/S0939-6411(03)00193-0).
- Burdett, J.K., Price, G.D., Price, S.L., 1982. Role of the crystal-field theory in determining the structures of spinels. *J. Am. Chem. Soc.* 104 (1), 92–95. <https://doi.org/10.1021/ja00365a019>.
- R. G. Burns, *Mineralogical Applications of Crystal Field Theory*, 2nd ed. Cambridge University Press, 1993. doi: 10.1017/CBO9780511524899.
- Chandradass, J., Balasubramanian, M., Kim, K.H., 2010. Size effect on the magnetic property of  $\text{CoAl}_2\text{O}_4$  nanopowders prepared by reverse micelle processing. *J. Alloy. Compd.* 506 (1), 395–399. <https://doi.org/10.1016/j.jallcom.2010.07.014>.
- Chen, Z.-Z. et al, 2004. Preparation of nanosized cobalt aluminate powders by a hydrothermal method. *Mater. Sci. Eng. B* 107 (2), 217–223. <https://doi.org/10.1016/j.mseb.2003.11.013>.
- Das, N.K. et al, 2020. Effect of substrate temperature on the properties of RF sputtered CdS thin films for solar cell applications. *Results Phys.* 17. <https://doi.org/10.1016/j.rinp.2020.103132>
- C. S. Dash et al., “Magnetic property applications of microwave method prepared zinc ion modified  $\text{CoAl}_2\text{O}_4$  nanoparticles.,” *Digest Journal of Nanomaterials & Biostructures (DJNB)*, vol. 16, no. 4, 2021.
- Davar, F., Salavati-Niasari, M., 2011. Synthesis and characterization of spinel-type zinc aluminate nanoparticles by a modified sol-gel method using new precursor. *J. Alloy. Compd.* 509 (5), 2487–2492. <https://doi.org/10.1016/j.jallcom.2010.11.058>.
- de la Calle, I., Soto-Gómez, D., Pérez-Rodríguez, P., López-Periago, J. E., 2019. Particle size characterization of Sepia Ink Eumelanin biopolymers by SEM, DLS, and AF4-MALLS: a comparative study. *Food Anal. Methods* 12 (5), 1140–1151. <https://doi.org/10.1007/s12161-019-01448-0>.
- Debnath, S., Das, R., 2020. Study of the optical properties of Zn doped Mn spinel ferrite nanocrystals shows multiple emission peaks in the visible range—a promising soft ferrite nanomaterial for deep blue LED. *J. Mol. Struct.* 1199. <https://doi.org/10.1016/j.molstruc.2019.127044>
- Desouza, L. et al, 2009. Blue pigments based on  $\text{Co}_x\text{Zn}_{1-x}\text{Al}_2\text{O}_4$  spinels synthesized by the polymeric precursor method. *Dyes Pigm.* 81 (3), 187–192. <https://doi.org/10.1016/j.dyepig.2008.09.017>.
- Duan, X., Pan, M., Yu, F., Yuan, D., 2011. Synthesis, structure and optical properties of  $\text{CoAl}_2\text{O}_4$  spinel nanocrystals. *J. Alloy. Compd.* 509 (3), 1079–1083. <https://doi.org/10.1016/j.jallcom.2010.09.199>.
- Dumitru, R. et al, 2017. Synthesis, characterization of nanosized  $\text{CoAl}_2\text{O}_4$  and its electrocatalytic activity for enhanced sensing application. *J. Therm. Anal. Calorim.* 128 (3), 1305–1312. <https://doi.org/10.1007/s10973-016-6045-y>.

- P. Durga Prasad and J. Hemalatha, "Enhanced magnetic properties of highly crystalline cobalt ferrite fibers and their application as gas sensors," *Journal of Magnetism and Magnetic Materials*, vol. 484, pp. 225–233, Aug. 2019, doi: 10.1016/j.jmmm.2019.04.026.
- Gingasu, D. et al, 2021. Mentha piperita-mediated synthesis of cobalt aluminate nanoparticles and their photocatalytic activity. *J. Mater. Sci. Mater. Electron.* 32 (8), 11220–11231.
- Grosso, D., 2011. How to exploit the full potential of the dip-coating process to better control film formation. *J. Mater. Chem.* 21 (43), 17033. <https://doi.org/10.1039/c1jm12837j>.
- Gul, I.H., Maqsood, A., Naeem, M., Ashiq, M.N., 2010. Optical, magnetic and electrical investigation of cobalt ferrite nanoparticles synthesized by co-precipitation route. *J. Alloy. Compd.* 507 (1), 201–206. <https://doi.org/10.1016/j.jallcom.2010.07.155>.
- Holmberg, J.P., Ahlberg, E., Bergenholtz, J., Hassellöv, M., Abbas, Z., 2013. Surface charge and interfacial potential of titanium dioxide nanoparticles: experimental and theoretical investigations. *J. Colloid Interface Sci.* 407, 168–176. <https://doi.org/10.1016/j.jcis.2013.06.015>.
- Hossain, M. et al, 2022. New analytical models for precise calculation of crystallite size: application to synthetic hydroxyapatite and natural eggshell crystalline materials. *Chem. Pap.*, 1–7
- Hossain, M.S., Ahmed, S., 2022. Synthesis of nano-crystallite gypsum and bassanite from waste Pila globosa shells: crystallographic characterization. *RSC Adv.* 12 (38), 25096–25105. <https://doi.org/10.1039/D2RA04881G>.
- Hossain, M., Hasan, M., Mahmud, M., Mobarak, M.B., Ahmed, S., 2022. Assessment of crystallite size of UV-synthesized hydroxyapatite using different model equations. *Chem. Pap.*, 1–9
- Hossain, M.S., Uddin, M.N., Sarkar, S., Ahmed, S., 2022. Crystallographic dependency of waste cow bone, hydroxyapatite, and  $\beta$ -tricalcium phosphate for biomedical application. *J. Saudi Chem. Soc.* 26, (6) 101559.
- Hossain, M.S., Tuntun, S.M., Bahadur, N.M., Ahmed, S., 2022. Enhancement of photocatalytic efficacy by exploiting copper doping in nano-hydroxyapatite for degradation of Congo red dye. *RSC Adv.* 12 (52), 34080–34094.
- Hossain, M.S., Uddin, M.N., Jahan, S.A., Ahmed, S., 2023. Synthesis and characterization of nano crystallite plaster of Paris prepared from waste eggshells and exploration of cytotoxicity, hemolysis and antimicrobial properties. *J. Mater. Chem. B.*
- Iakovleva, M. et al, 2015. Ground state and low-energy magnetic dynamics in the frustrated magnet  $\text{CoAl}_2\text{O}_4$  as revealed by local spin probes. *Phys. Rev. B* 91, (14). <https://doi.org/10.1103/PhysRevB.91.144419>
- Ianoş, R., Borcănescu, S., Lazău, R., 2014. Large surface area  $\text{ZnAl}_2\text{O}_4$  powders prepared by a modified combustion technique. *Chem. Eng. J.* 240, 260–263. <https://doi.org/10.1016/j.cej.2013.11.082>.
- Irfan, H., Mohamed Racik, K., Anand, S., 2018. X-ray peak profile analysis of  $\text{CoAl}_2\text{O}_4$  nanoparticles by Williamson-Hall and size-strain plot methods. *MoEM* 4 (1), 31–40. <https://doi.org/10.3897/j.moem.4.1.33272>.
- Jüstel, T., Nikol, H., Ronda, C., 1998. New developments in the field of luminescent materials for lighting and displays. *Angew. Chem. Int. Ed.* 37 (22), 3084–3103. [https://doi.org/10.1002/\(SICI\)1521-3773\(19981204\)37:22<3084::AID-ANIE3084>3.0.CO;2-W](https://doi.org/10.1002/(SICI)1521-3773(19981204)37:22<3084::AID-ANIE3084>3.0.CO;2-W).
- Kafashan, H., 2018. Structural characterizations of pure SnS and Indoped SnS thin films using isotropic and anisotropic models. *Mater. Res. Express* 5, (4). <https://doi.org/10.1088/2053-1591/aabdb8> 046417.
- Kurajica, S., Popović, J., Tkalčec, E., Gržeta, B., Mandić, V., 2012. The effect of annealing temperature on the structure and optical properties of sol-gel derived nanocrystalline cobalt aluminate spinel. *Mater. Chem. Phys.* 135 (2–3), 587–593. <https://doi.org/10.1016/j.matchemphys.2012.05.030>.
- Leila, D., Mar, L.-G., Fatima, B., Abdelyamine, N., Ali, B., Nacereddine, H., 2018. Effect of polyethylene glycol and propyltrimethoxysilane on structural and optical properties of zinc oxide nanoparticles synthesized by sol-gel process. *J. Theor. Appl. Phys.* 12 (3), 159–167. <https://doi.org/10.1007/s40094-018-0303-2>.
- Lewis, P.A. (Ed.), 1988. *Pigment Handbook*. 2nd ed. Wiley, New York.
- V. Madhavi, T. N. V. K. V. Prasad, A. V. B. Reddy, B. Ravindra Reddy, and G. Madhavi, "Application of phyto-genic zerovalent iron nanoparticles in the adsorption of hexavalent chromium," *Spectrochimica Acta Part A: Molecular and Biomolecular Spectroscopy*, vol. 116, pp. 17–25, Dec. 2013, doi: 10.1016/j.saa.2013.06.045.
- Majid, F. et al, 2020. Effect of hydrothermal reaction time on electrical, structural and magnetic properties of cobalt ferrite. *Z. Phys. Chem.* 234 (2), 323–353. <https://doi.org/10.1515/zpch-2019-1423>.
- Mazzoli, A., Favoni, O., 2012. Particle size, size distribution and morphological evaluation of airborne dust particles of diverse woods by scanning electron microscopy and image processing program. *Powder Technol.* 225, 65–71. <https://doi.org/10.1016/j.powtec.2012.03.033>.
- Melo, D.M.A., Cunha, J.D., Fernandes, J.D.G., Bernardi, M.I., Melo, M.A.F., Martinelli, A.E., 2003. Evaluation of  $\text{CoAl}_2\text{O}_4$  as ceramic pigments. *Mater. Res. Bull.* 38 (9–10), 1559–1564. [https://doi.org/10.1016/S0025-5408\(03\)00136-3](https://doi.org/10.1016/S0025-5408(03)00136-3).
- Mindru, I. et al, 2017.  $\text{Tb}^{3+}$ -doped alkaline-earth aluminates: Synthesis, characterization and optical properties. *Mater. Res. Bull.* 85, 240–248.
- Mindru, I. et al, 2019. A new approach: synthesis of cobalt aluminate nanoparticles using tamarind fruit extract. *Mater. Sci. Eng. B* 246, 42–48.
- Mohammed, A.A., Khodair, Z.T., Khadom, A.A., 2020. Preparation and investigation of the structural properties of  $\alpha\text{-Al}_2\text{O}_3$  nanoparticles using the sol-gel method. *Chem. Data Collect.* 29, <https://doi.org/10.1016/j.cdc.2020.100531> 100531.
- Mote, V., Purushotham, Y., Dole, B., 2012. Williamson-Hall analysis in estimation of lattice strain in nanometer-sized  $\text{ZnO}$  particles. *J. Theor. Appl. Phys.* 6 (1), 6. <https://doi.org/10.1186/2251-7235-6-6>.
- Pan, Z., Wang, Y., Huang, H., Ling, Z., Dai, Y., Ke, S., 2015. Recent development on preparation of ceramic inks in ink-jet printing. *Ceram. Int.* 41 (10), 12515–12528. <https://doi.org/10.1016/j.ceramint.2015.06.124>.
- Peymannia, M., Soleimani-Gorgani, A., Ghahari, M., Najafi, F., 2014. Production of a stable and homogeneous colloid dispersion of nano  $\text{CoAl}_2\text{O}_4$  pigment for ceramic ink-jet ink. *J. Eur. Ceram. Soc.* 34 (12), 3119–3126. <https://doi.org/10.1016/j.jeurceramsoc.2014.03.022>.
- Prabhakar, R., Samadder, S.R., 2018. Low cost and easy synthesis of aluminium oxide nanoparticles for arsenite removal from groundwater: a complete batch study. *J. Mol. Liq.* 250, 192–201. <https://doi.org/10.1016/j.molliq.2017.11.173>.
- Quirino, M.R., Oliveira, M.J.C., Keyson, D., Lucena, G.L., Oliveira, J.B.L., Gama, L., 2016. Synthesis of zinc aluminate with high surface area by microwave hydrothermal method applied in the transesterification of soybean oil (biodiesel). *Mater. Res. Bull.* 74, 124–128. <https://doi.org/10.1016/j.materresbull.2015.10.027>.
- Ragupathi, C., Vijaya, J.J., Kennedy, L.J., 2014. Synthesis, characterization of nickel aluminate nanoparticles by microwave combustion method and their catalytic properties. *Mater. Sci. Eng. B* 184, 18–25. <https://doi.org/10.1016/j.mseb.2014.01.010>.
- Ravikumar, B.S., Nagabhushana, H., Sharma, S.C., Vidya, Y.S., Anantharaju, K.S., 2015. Calotropis procera mediated combustion synthesis of  $\text{ZnAl}_2\text{O}_4:\text{Cr}^{3+}$  nanophosphors: structural and luminescence studies. *Spectrochim. Acta A Mol. Biomol. Spectrosc.* 136, 1027–1037. <https://doi.org/10.1016/j.saa.2014.09.126>.
- Salavati-Niasari, M., Farhadi-Khouzani, M., Davar, F., 2009. Bright blue pigment  $\text{CoAl}_2\text{O}_4$  nanocrystals prepared by modified sol-gel method. *J. Sol-Gel Sci. Technol.* 52 (3), 321–327. <https://doi.org/10.1007/s10971-009-2050-y>.

- Salem, S., 2014. Effect of calcination temperature on colorant behavior of cobalt-aluminate nano-particles synthesized by combustion technique. *J. Ind. Eng. Chem.* 20 (3), 818–823. <https://doi.org/10.1016/j.jiec.2013.06.011>.
- Salem, S.H., Jazayeri, S.H., Bondioli, F., Allahverdi, A., Shirvani, M., 2011. Characterizing thermal behavior of ceramic glaze containing nano-sized cobalt-aluminate pigment by hot stage microscopy. *Thermochim. Acta* 521 (1–2), 191–196. <https://doi.org/10.1016/j.tca.2011.04.023>.
- Salem, S., Jazayeri, S.H., Bondioli, F., Allahverdi, A., Shirvani, M., Ferrari, A.M., 2012. CoAl<sub>2</sub>O<sub>4</sub> nano pigment obtained by combustion synthesis. *Int. J. Appl. Ceram. Technol.* 9 (5), 968–978. <https://doi.org/10.1111/j.1744-7402.2011.02704.x>.
- Sen, S.K. et al, 2020. X-ray peak profile analysis of pure and Dy-doped  $\alpha$ -MoO<sub>3</sub> nanobelts using Debye-Scherrer, Williamson-Hall and Halder-Wagner methods. *Adv. Nat. Sci: Nanosci. Nanotechnol.* 11, (2). <https://doi.org/10.1088/2043-6254/ab8732> 025004.
- Sen, S.K., Paul, T.C., Dutta, S., Hossain, M.N., Mia, M.N.H., 2020. XRD peak profile and optical properties analysis of Ag-doped h-MoO<sub>3</sub> nanorods synthesized via hydrothermal method. *J. Mater. Sci.: Mater. Electron.* 31 (2), 1768–1786. <https://doi.org/10.1007/s10854-019-02694-y>.
- Sharma, R.K., Ghose, R., 2014. Synthesis and characterization of nanocrystalline zinc aluminate spinel powder by sol-gel method. *Ceram. Int.* 40 (2), 3209–3214. <https://doi.org/10.1016/j.ceramint.2013.09.121>.
- Song, Y., Zheng, Y.L., Tang, Y.F., Yang, H.B., 2017. Fabrication and stability of CoAl<sub>2</sub>O<sub>4</sub> ceramic pigment for 3D printing. *MSF* 898, 1935–1939. <https://doi.org/10.4028/www.scientific.net/MSF.898.1935>.
- Srisawad, N., Chaitree, W., Mekasuwandumrong, O., Praserttham, P., Panpranot, J., 2012. Formation of CoAl<sub>2</sub>O<sub>4</sub> nanoparticles via low-temperature solid-state reaction of fine gibbsite and cobalt precursor. *J. Nanomater.* 2012, 1–8. <https://doi.org/10.1155/2012/108369>.
- Stokes, A.R., Wilson, A.J.C., 1944. The diffraction of X rays by distorted crystal aggregates - I. *Proc. Phys. Soc.* 56 (3), 174–181. <https://doi.org/10.1088/0959-5309/56/3/303>.
- F. M. Stringhini, E. L. Foletto, D. Sallet, D. A. Bertuol, O. Chivavone-Filho, and C. A. O. do Nascimento, "Synthesis of porous zinc aluminate spinel (ZnAl<sub>2</sub>O<sub>4</sub>) by metal-chitosan complexation method," *Journal of Alloys and Compounds*, vol. 588, pp. 305–309, Mar. 2014, doi: 10.1016/j.jallcom.2013.11.078.
- Taguchi, M. et al, 2013. Reaction temperature variations on the crystallographic state of spinel cobalt aluminate. *Dalton Trans.* 42 (19), 7167. <https://doi.org/10.1039/c3dt32828g>.
- Tang, Q. et al, 2017. Preparation and characterization of nanoscale cobalt blue pigment for ceramic inkjet printing by sol-gel self-propagating combustion. *Mat. Res.* 20 (5), 1340–1344. <https://doi.org/10.1590/1980-5373-mr-2017-0322>.
- Tielens, F., Calatayud, M., Franco, R., Recio, J.M., Pérez-Ramírez, J., Minot, C., 2006. Periodic DFT study of the structural and electronic properties of bulk CoAl<sub>2</sub>O<sub>4</sub> spinel. *J. Phys. Chem. B* 110 (2), 988–995. <https://doi.org/10.1021/jp053375l>.
- Tong, Y., Zhang, H., Wang, S., Chen, Z., Bian, B., 2016. Highly dispersed re-doped CoAl<sub>2</sub>O<sub>4</sub> nanopigments: synthesis and chromatic properties. *J. Nanomater.* 2016, 1–7. <https://doi.org/10.1155/2016/4169673>.
- Tuntun, S.M., Hossain, M.S., Uddin, M.N., Shaikh, M.A.A., Bahadur, N.M., Ahmed, S., 2023. Crystallographic characterization and application of copper doped hydroxyapatite as a biomaterial. *New J. Chem.* <https://doi.org/10.1039/D2NJ04130H>.
- Venkatalaxmi, A., Padmavathi, B.S., Amaranath, T., 2004. A general solution of unsteady Stokes equations. *Fluid Dyn. Res.*, 9
- Venkatesan, A. et al, 2022. Synthesis, characterization and magnetic properties of Mg<sup>2+</sup> doped green pigment Cobalt aluminate nanoparticles. *J. Mater. Sci.: Mater. Electron.* 33 (27), 21246–21257. <https://doi.org/10.1007/s10854-022-08834-1>.
- Visinescu, D., Jurca, B., Ianculescu, A., Carp, O., 2011. Starch – a suitable fuel in new low-temperature combustion-based synthesis of zinc aluminate oxides. *Polyhedron* 30 (17), 2824–2831. <https://doi.org/10.1016/j.poly.2011.08.006>.
- Wang, Q., Chang, Q., Wang, Y., Wang, X., Zhou, J., 2016. Ultrafine CoAl<sub>2</sub>O<sub>4</sub> ceramic pigment prepared by Pechini-sacrificial agent method. *Mater. Lett.* 173, 64–67. <https://doi.org/10.1016/j.matlet.2016.03.014>.
- Wang, C., Liu, S., Liu, L., Bai, X., 2006. Synthesis of cobalt–aluminate spinels via glycine chelated precursors. *Mater. Chem. Phys.* 96 (2–3), 361–370. <https://doi.org/10.1016/j.matchemphys.2005.07.066>.
- Xu, L. et al, 2015. One-step synthesis of ordered mesoporous CoAl<sub>2</sub>O<sub>4</sub> spinel-based metal oxides for C<sub>2</sub>O reforming of C<sub>H</sub>4. *RSC Adv.* 5 (60), 48256–48268. <https://doi.org/10.1039/C5RA07249B>.
- Yadav, H., Sinha, N., Goel, S., Kumar, B., 2016. Eu-doped ZnO nanoparticles for dielectric, ferroelectric and piezoelectric applications. *J. Alloy. Compd.* 689, 333–341. <https://doi.org/10.1016/j.jallcom.2016.07.329>.
- Zaharko, O. et al, 2014. Unconventional magnetic order in the frustrated diamond-lattice antiferromagnet CoAl<sub>2</sub>O<sub>4</sub> studied by neutron diffraction and classical Monte Carlo simulation. *Phys. Rev. B* 90, (13). <https://doi.org/10.1103/PhysRevB.90.134416> 134416.
- Zayat, M., Levy, D., 2000. Blue CoAl<sub>2</sub>O<sub>4</sub> particles prepared by the sol-gel and citrate-gel methods. *Chem. Mater.* 12 (9), 2763–2769. <https://doi.org/10.1021/cm001061z>.
- Zhang, A., Mu, B., Luo, Z., Wang, A., 2017. Bright blue halloysite/CoAl<sub>2</sub>O<sub>4</sub> hybrid pigments: preparation, characterization and application in water-based painting. *Dyes Pigm.* 139, 473–481. <https://doi.org/10.1016/j.dyepig.2016.12.055>.